communications medicine

A Nature Portfolio journal

Article

https://doi.org/10.1038/s43856-025-00809-7

Mini-GRID therapy delivers optimised spatially fractionated radiation therapy using a flattening free filter accelerator

M. Isabel Acuña[1], Charlotte Lamirault[2], Thibaut Larcher[3], Elise Brisebard[3], Tim Schneider[4,5], Marjorie Juchaux[4,5], Ramon Iglesias-Rey[6], Sabela Fernández-Rodicio[6], Pablo Aguiar[7], Noemi Gómez-Lado[7], Immaculada Martínez-Rovira[8], Roberto González-Vegas[8], Ibraheem Yousef[9], Antonio Gomez-Caamano[10], Miguel Pombar[11], Victor Luna[11], Manuel Sanchez[11] & Yolanda Prezado[1,4,5,12]

Abstract

Background Radioresistant tumours remain a challenge for conventional radiation therapy (RT), and often, only palliative treatment can be offered. Recently developed techniques, such as spatially fractionated radiation therapy (SFRT) could potentially improve treatment. However, current clinical SFRT implementations do not allow the full potential to be exploited. We further optimize SFRT, developing mini-GRID, which uses a flattening free filter accelerator.

Methods The increase in normal tissue tolerances provided by mini-GRID compared to conventional RT and GRID therapy was validated in a rat model of brain irradiation in a longitudinal imaging study, behavioural tests and by histopathological evaluation.

Results The implementation optimizes mini-GRID therapy, with beam widths around 2 mm^2. The peak-to-valley dose ratios and peak dose rates are around 4 and 7 Gy/min, respectively. Mini-GRID RT allows the use of high peak doses: 42 Gy in one fraction, a factor more than twice higher than the peak doses generally employed in conventional GRID therapy (20 Gy peak dose). This enables the use of more aggressive and potentially curative treatments. Infrared microspectroscopy analysis suggests different early biochemical changes in both modalities, with conventional RT leading to stronger modifications in the secondary protein structure, and higher oxidative damage than mini-GRID RT.

Conclusions The possibility to treat both large and small tumours, and to perform safe and potentially curative dose escalations in previously untreatable cases, makes mini-GRID a promising approach to expand the clinical use of SFRT.

Plain language summary

Conventional radiation therapy is used to shrink tumours, however, in some cases, tumours become resistant to radiation, resulting in limited treatment options. To overcome this, we have developed a radiation therapy technique, called mini-GRID therapy that can target these hard-to-treat tumours. Mini-GRID therapy does this by distributing the dose of radiation across the tissue instead of localized to one spot, allowing for a higher dose to be applied. Here, we demonstrate the feasibility and reduction of side effects on normal tissues using rat brain tissue following mini-GRID therapy. Our results show that the mini-GRID has the potential to improve radiation therapy in tumours that are resistant to radiation or require a higher dose to reduce tumour size without affecting normal tissue. This could provide a treatment strategy for currently untreatable brain tumours.

The treatment of many late-stage tumours, radio-resistant bulky tumours[1], recurring tumours[2], large brain tumours[3–6] and some paediatric cancers[7,8] remains a challenge since it is still compromised by the normal tissue tolerances. Unconventional approaches, such as spatially fractionated radiation therapy (SFRT)[9], can lead to remarkably increased normal tissue dose tolerances and high therapeutic ratios, even in those difficult-to-treat cases[10–12]. Out of the four main types of SFRT[9], GRID[13] and Lattice therapy (LRT)[14] were employed in the treatments of more than 500 patients at medical linear accelerators (LINACS), mainly with advanced disease and palliative intention[13,15–19]. The other two techniques are microbeam radiation therapy (MRT) and minibeam radiation therapy (MBRT)[9], both using submillimetric beams. The first patients (compassionate treatments) have been recently treated with MBRT[20]. Despite the advantages observed[9], different implementations are needed to unleash the full potential of SFRT. Indeed, the current implementations of GRID and LRT therapy face some limitations. Firstly, the important lateral scattering of the 6 MV X-rays beams used in conventional LINACS leads to high valley doses, which do not favour normal tissue sparing[21]. Another drawback is the need for "large"

A full list of affiliations appears at the end of the paper. e-mail: Yolanda.prezado@usc.es

beam sizes (around 1 cm^2) to retain an acceptable dose rate in the case of GRID therapy or to have enough precision with the multileaf collimator in the case of LRT. This implies that only large tumours can be treated with GRID or LRT.

The use of narrower beams (<2–3 mm^2) would allow exploiting the dose-volume effects[22], thus enabling the use of higher and therapeutic doses in radioresistant tumours. It would also allow the treatment of smaller tumours than with classical clinical SFRT[23–26]. Along that line, a previous in-silico study showed that the use of flattening free filter (FFF) accelerators could overcome all those limitations[27]. The removal of the flattening filter shifts the beam energy spectrum towards lower energies, reducing lateral scattering and lowering, consequently, the valley doses in normal tissues. In addition, photon fluence would be increased by a factor 2-3 largely compensating for the loss of dose rate if small grid sizes are to be used[27]. Finally, beam widths narrower than 3 mm^2 were shown to be theoretically achievable, potentially increasing the normal tissue tolerances[22]. In this work, we have implemented an optimized SFRT technique employing narrow beams (≤2 mm^2) at 6FFF TrueBeam accelerator. It will be referred to as "mini-GRID" hereafter. The increase in normal tissue tolerances provided by this new technique with respect to conventional RT and GRID therapy was validated in a rat model (brain irradiation) by means of a longitudinal imaging study, behavioural tests and histopathology evaluations. This new avenue has not been explored in any centre yet, and it might dramatically reduce the upfront investment in SFRT, easing the spread of SFRT and positioning SFRT as a curative option.

The main findings of this study are the following: (i) an optimised implementation of mini-GRID therapy with beam widths of around 2 mm^2 is achieved; (ii) mini-GRID RT allows the use of peak doses a factor more than twice higher than the peak doses generally employed in conventional GRID therapy (20 Gy peak dose). This enables the use of more aggressive and potentially curative treatments; (iii) mini-GRID RT results in less modifications in the secondary protein structure, and lower oxidative damage as compared with conventional RT.

Methods

Technical implementation and dosimetry

The new mini-GRID technique was implemented at a 6 MV VARIAN True Beam flattening free filter linear accelerator[28]. Suitable collimators were designed by means of Monte Carlo (MC) simulations (TOPAS toolkit, version 3.6 based on Geant4 version 4.10.7). The use of the multileaf collimator is not suitable due to the lack of precision and penumbra impact in the narrow fields to be achieved (≤2 mm^2). For the collimator design, phase-space files from VARIAN have been used as input of the MC simulations. We manufactured the collimator in steel (10 cm thickness) using electro-discharge machinery, ensuring hole widths of 1.1 mm at its entrance. This leads to the formation of a grid dose pattern, featuring beam widths and centre-to-centre (ctc) distances of 1.8 mm and 3.7 mm, respectively, at a depth of 1 cm within a water phantom.

The phantom surface was placed at the isocentre. The holes followed a tilt equalling the angular spread. The collimator is attached to the gantry head by using a Brainlab holder as shown in Fig. S1 in supplemental materials.

The resulting mini-GRID dose distributions were assessed by means of Monte Carlo simulations and gafchromic films (EBT-XD), with the same methodology as previous studies in MBRT[29].

Animal irradiations

The Bioethics Committee of the Universidad de Santiago de Compostela approved the animal studies. All studies were conducted in accordance with the animal welfare and ethical guidelines of Spanish national law (RD 53/2013). The present study is reported following ARRIVE guidelines.

The brains of naive 7-weeks-old male Fischer rats (F344, Janvier Labs, France) were irradiated. Rats' brain volume is around 2002 ± 64 mm^3[30]. The animals were hosted at "Centro de Biomedicina Experimental de Santiago de Compostela" (CEBEGA). Rats were housed in groups in a temperature and humidity-controlled room (12:12 light/dark cycle) with ad libitum access to water and food. They were acclimatized, at least, for one week before beginning studies.

We included rats of only one sex (male) to minimise the number of animals in this first proof-of-concept experiment. The choice of males was motivated by the fact that the incidence and outcome of glioblastoma differ between sexes, occurring 1.6 times more frequently in males than in females, who also have better outcomes[31].

Three groups of animals were considered: a control group, a group receiving conventional radiotherapy (conv. RT) and a third group receiving mini-GRID therapy (mini-GRID RT) For irradiations, the rats were anesthetized by isoflurane (Isoflutek, 1000 mg/g) inhalation (4% induction), and placed on the surgical bed (2.5% isoflurane maintenance). Portal imaging for positioning fine-tuning was used. The central part of the brain (1 × 1 cm^2) was irradiated (lateral irradiations) in one fraction. Gafchromic films placed at the animals' skin were employed for quality control. A dose escalation study was performed. The prescription doses were 20 ± 1 Gy (N = 18/group, corresponding to 42 ± 3 and 9.8 ± 0.8 Gy peak and valley doses in the mini-GRID case) or 25 ± 1 Gy (N = 15/group, corresponding to 55 ± 4 and 12.7 ± 1.0 Gy peak and valley doses, in the mini-GRID case). Gy refers to Gray. Those correspond to mean dose at approximately the middle of the rat's brain (1 cm-depth) calculated in the area between the two most extreme peaks[32]. Table S1 in supplemental materials shows the prescribed dose at 1 cm depth in the different groups.

Animals were followed up for a period of 6 months. We performed behavioural tests on 10 animals per group. Additionally, 5 animals per group followed a longitudinal study including magnetic resonance (MRI) and positron emission tomography (PET) imaging. Three animals were added to the groups receiving 20 Gy and sacrificed 48 h after irradiation for infrared microspectroscopy studies.

We euthanized the animals at the end of each study (6 months after irradiation) and extracted their brains for anatomopathological evaluations. Eight and nine brains per group were analysed in groups receiving 20 and 25 Gy, respectively.

Animals follow up

The health status of each rat was checked five times per week. The relative weight compared with that on the day of irradiation was calculated.

Longitudinal imaging evaluations

Whole-body positron emission/computer tomography (PET/CT) images were acquired at a Bruker Albira microPET/CT after injection of 0.3 mCi of ^{18}F-FDG (2-deoxy-2-(*18F*) fluoro-D-glucose (*FDG*)). The acquisitions took place 3 days before irradiation (basal), 3, 30 and 105 days after irradiation. The subsequent analysis was on the brain, using anatomical templates (Schiffer) and PMOD v.4.2 software (PMOD Technologies, Zürich, Switzerland), for studying metabolism changes in different brain areas over time.

Magnetic resonance studies were conducted on a Bruker Biospec 9.4 T MR scanner (horizontal bore magnet with 12 cm wide Bruker BioSpin) equipped with actively shielded gradients (440 mT m^{-1}). Animals were imaged with a combination of a linear birdcage resonator (7 cm in diameter) for signal transmission and a 2 × 2 surface coil array for signal detection, positioned over the head of the animal, which was fixed with a teeth bar, earplugs, and adhesive tape. Transmission and reception coils were actively decoupled from each other.

A longitudinal assessment of brain lesions, oedema, inflammation, T2 and T2* relaxation values, and the presence of haemorrhages or micro-haemorrhages in the study groups was conducted using T2- and T2*-weighted MRI at baseline (before radiation) and at 2- and 30-days post-radiation. For this purpose, T2-maps calculated from T2-weighted images (T2-WI) using a MSME sequence (axial orientation): with an echo time (ET) = 9 ms, repetition time (RT) = 3 sec, 16 echoes with 9 ms echo spacing, flip angle (FA) = 180°, NA = 2, spectral bandwidth (SW) = 75 KHz, 14 slices of 1 mm, 19.2 × 19.2 mm^2 FOV (with saturation bands to suppress signal outside this FOV), a matrix size of 192 × 192 (isotropic in-plane resolution

of 100 µm/pixel) and implemented without fat suppression option. T2*-maps calculated from T2*-weighted images (T2*-WI) using a MGE sequence (axial orientation): with an ET = 2.9 ms, RT = 1.5 s, 16 echoes with 3.8 ms echo spacing, flip angle (FA) = 50°, NA = 1, spectral bandwidth (SW) = 75 KHz, 14 slices of 1 mm, 19.2 × 19.2 mm^2 FOV (with saturation bands to suppress signal outside this FOV), a matrix size of 192 × 192 (isotropic in-plane resolution of 100 μm^2/pixel) and implemented without fat suppression option.

At 6 months post-radiation, a brain volumetry study was conducted using T2-WI using a RARE (Rapid Acquisition with Relaxation Enhancement) sequence (axial and coronal orientations): with an ET = 11 ms, RT = 2.5 sec, Rare Factor (RF) = 8, flip angle (FA) = 180°, NA = 3, spectral bandwidth (SW) = 37 KHz, 14 slices of 1 mm, 25.6 × 25.6 mm^2 FOV, a matrix size of 256 × 256 (isotropic in-plane resolution of 100 μm^2/pixel) and implemented without fat suppression option

Fourier Transform Infrared Microspectroscopy

To complement the PET analysis and dive deeper into potential biochemical changes, Fourier Transform Infrared Microspectroscopy (FTIRM) was used. FTIRM is a powerful, label-free and non-destructive tool for examining biological samples[33], enabling the measurement of changes in the vibrational modes of the molecules that are infrared active. Thus, it provides information about the composition, molecular structure and chemical modifications of the main biomolecules (nucleic acids, carbohydrates, proteins and lipids). Therefore, FTIRM can be used as a kind of probe to get global insights into the biochemical fingerprint of the structure and function of the tissue and how this change as a function of the irradiation mode[34–36]. The potential distinct early radiochemical changes observed in the cells depending on the RT technique might help explain the triggering of some more macroscopy effects, such as vascular or immunomodulatory effects, which could be assessed by immunochemistry at a later stage.

At 48 h post-RT, the whole brain was snap-frozen in isopentane and cooled in liquid nitrogen. Prior to the FTIRM measurements, 5 µm-thick brain cryosections were deposited onto low-e microscope slides (Kevley Technologies). We immersed the sections in zinc formalin solution (Sigma-Aldrich), rinsed them with Millipore ultrapure water, and then dried them. We performed FTIRM measurements at the MIRAS beamline of ALBA Synchrotron, using the BRUKER 3000 hyperion microscope in conjunction with a Vertex 70 spectrometer. We collected raster scanning maps of the whole mouse brain section for each sample condition. Infrared spectra were acquired in the mid-infrared range with a 100×100 μm^2 resolution after 4 co-added scans with a 4 cm^{-1} spectral resolution.

The probability density of the data for several spectral ratios was used as specific markers for indices of biochemical changes. We evaluated chemical maps and violin plots, which show the distribution of relative intensities of the ratios as a function of the irradiation configuration. We obtained chemical mapping by integrating infrared signals in different spectral domains, prior to baseline. We looked at the Amide I (AI, 1714–1585 cm^{-1}), Amide II (AII, 1585–1483 cm^{-1}), Phosphate I (PhI, 1270–1186 cm^{-1}), and Phosphate II (PhII, 1135–1004 cm^{-1}), as well as the C=O carbonyl ester stretching vibrations from phospholipids (1760–1718 cm^{-1}), in the 1800–950 cm^{-1} range. We also assessed the asymmetric methylene aCH2 (2945–2900 cm^{-1}) to the asymmetric methyl aCH3 (2980–2945 cm^{-1}) spectral ratio.

Behavioural tests

Naive rats were housed in groups of two or three animals per cage in a temperature- and humidity-controlled colony room and maintained on a 12:12-h light/dark cycle with *ad libitum* access to water and food. The same researcher performed all behavioural tests at approximately the same time each day for each animal to avoid sleep cycle disruption.

The open field test (OF) was adopted as a basal assessment to measure locomotor, exploratory activity, and general anxiety. Memory capacity was assessed using the novel object recognition task (ORT). In the OF test[37], each rat was placed in an open arena (1 m x 1 m) and allowed to freely explore for 5 min. The experimental room features low light (maximum 30 lux) and 60 dB of background noise. We found an inverse correlation between anxiety and the time the rat spent in the arena's centre. Each animal was placed in the OF arena two times per day (5 min, 5 min) with an interval of 3 h between each trial. The rat's anxiety inversely correlated with the amount of time it spent in the arena's centre. The total distance travelled, the time spent rearing, and the time spent in the centre were recorded. We analysed the open field tests using the ANY-maze software (Stoelting).

We performed the novel object recognition task (NOR) to evaluate the rats' ability to recognize a novel object or location in a known environment. We allowed each rat to familiarize itself with two identical objects in the OF arena once for 5 min. Three hours later, we placed the rat in the OF arena for 3 min, exposing it to either one novel object (ORT), the same object in a new location (OLT), or the same familiar object in the same location. The time spent exploring each object was measured and used to calculate the discrimination ratio ([time exploring the novel object or the novel location of the object—time spent exploring the familiar object or location]/time spent exploring both objects). We conducted these tests four times: 48 h before irradiation, followed by 1, 3, and 6 months after irradiation.

Motor coordination and muscle tone were assessed by measuring the fall latency on the Rotarod (Ugo Basile, Varese, Italy). Rats are placed on a Rotarod and first pre-trained on the apparatus for 2 cycles at 10 min intervals at constant speed at 4 rpm for 2 min. After training (30–60 min later), animals are replaced in a Rotarod for the test. The rats were subjected to 3 trials/day.

We gradually increased the rotation speed from 4 to 40 rpm for a maximum of 5 min, with a rest interval of 10 min between trials. The latency (in seconds) of falling was recorded. The normal animal will try to keep its balance on the rod. We assessed the animals 1, 3, and 6 months after irradiation.

Histopathology

At the end of the study period (6 months after irradiation), animals were humanely euthanised by CO_2 asphyxia.

Whole brains were removed and fixed in zinc-formalin (Sigma-Aldrich Intl GmbH, Germany) for 3 days before being transferred to ethanol for histopathological analyses. Brains were then cut into six coronal sections using a method adapted from the Society of Toxicologic Pathology's guidelines[38] prefrontal cortex, striatum, thalamus, pons, cerebellum, medulla oblongata) and embedded in paraffin. We took three 4 µm-thick serial sections from each paraffin block to stain with Hematoxylin Eosin Saffron (HES) and to label with immunohistochemistry (IHC) to look for microglia (Iba-1, 1:4000, 013-27691, Wako Chemicals, RRID: AB_2934095) and astrocytes (GFAP, 1:2500, Z0334, Dako, RRID: AB_10013382). Tissue sections were deparaffinized and rehydrated prior to processing in an automaton (Roche Discovery Ultra). Briefly, antigen retrieval (AR) by heating for 40 min at 98 °C (Iba-1) or 95 °C (GFAP) in Cell Conditioning Solution buffer (CC1, Roche). Next, we incubated the slides with the blocking solution (110, Diagomics) for 30 min at 37 °C, and then we diluted the primary antibody in Ab diluent (Ventana, Tucson, Arizona) for 1 h at 37 °C. We rinsed the slides and then incubated them with a biotinylated goat anti-rabbit IgG antibody (E0432, Dako) at a 1:200 dilution for 30 min at 37 °C. After washing, we incubated the slides with streptavidin/HRP (434323, Invitrogen) at a 1:200 dilution for 30 min at 37 °C. Finally, we washed, counterstained, dehydrated, and mounted the slides.

A trained, board-certified veterinary pathologist performed all histopathological assessments blindly. Four histopathological parameters were semi-quantitatively scored on HES-stained sections: (i) necrosis using a 4-step scale (0 = no lesion, 1 = degeneration of some isolated neuron; 2 = focal necrosis; 3 = extensive and/or multifocal necrosis); (ii) mineralization using a 3-step scale (0 = no lesion, 1 = a few (<5) small mineral deposits; 2 = extensive and/or multifocal mineralization); (iii) choroid plexus changes using a 4-step scale (0 = no lesion, 1 = pigment deposit; 2 = mild thickening with amyloid-like material; 3 = marked amyloid-like deposit with epithelial cell necrosis); (iv) intracellular lipofuscin deposit with a 3-step scale (0 = no lesion, 1 = less than 5 cells with pigments; 2 = many cells with pigments). 2 additional parameters, (i) microgliosis and (ii) astrocytosis, were scored on IHC sections, labelled respectively with an anti-Iba1 and an anti-GFAP antibody. For these 2 last parameters, a

4-step scale was used (0 = no change, 1 = mild focal; 2 = marked focal; 3 = extensive and/or multifocal marked or severe labelling). Eventually, an individual cumulative composite score was calculated by summing all 6 scores previously described (for a total ranging from 0 to 16).

Statistics and reproducibility

The sample size ($N = 10$ for behavioural tests, $N = 5$ for the imaging studies and $N = 3$ for FTIRM) was calculated using G*Power to achieve a statistical power of up to 75%. For the FTIRM analysis R programme was used. The non-parametric Kruskal-Wallis test was employed to evaluate the significance between groups. Then, when group effects were found to be statistically significant, a Dunn test for pairwise comparisons, including the Bonferroni adjustment, was performed. For the analysis of behavioural tests and weight curves statistical analyses (two-way ANOVA, a significance threshold set at 0.05) were performed using GraphPad Prism version 10.1. for Windows (GraphPad Software, San Diego CA, United States, www.graphpad.com)

Results

Dosimetry characterization

Table 1 shows the dosimetry characteristics assessed by both MC and gafchromic films in a solid water phantom with the surface placed in the isocentre. A good global agreement is found. Beam widths, FWHM and ctc remain almost constant as a function of depth. Figure S1 in supplemental materials shows a photograph of an irradiated gafchromic film and a dose heat map.

The peak dose rate is 6.8 Gy/min at 1 cm depth.

Monte Carlo simulations were performed in computer tomography images of a rat head to assess the calibration factor between the dose in the solid water and the dose in the rat brain for the irradiation field used (1 cm × 1 cm). A negligible factor is obtained.

Table 1 | Dosimetry parameters (mean ± SD). PVDR refers to peak-to-valley dose ratio, CTC to centre-to-centre distance, and FWHM to full width half-at-maximum. Uncertainty bars correspond to type B uncertainties

	Measurements			Monte Carlo
Depth (cm)	PVDR	CTC (mm)	FWHM (mm)	PVDR
1	4.3 ± 0.2	3.6 ± 0.1	1.8 ± 0.1	4.1 ± 0.05
2	4.0 ± 0.2	3.6 ± 0.1	1.9 ± 0.1	3.8 ± 0.05
3	3.9 ± 0.2	3.7 ± 0.1	1.9 ± 0.1	3.7 ± 0.05
4	3.8 ± 0.2	3.7 ± 0.1	2.0 ± 0.1	3.5 ± 0.05

Clinical symptoms

All animals gained weight during the study. No statistically significant weight differences were found among the controls and the groups irradiated at 20 Gy (Fig. 1a) In contrast, the groups irradiated at 25 Gy show a significant weight gain difference with respect to the controls (Conv. RT ($F(1, 17) = 7.741$ $p = 0.0128$) and mini-GRID RT ($F(1, 17) = 5.994$, $p = 0.0255$) (Fig. 1b). All irradiated rats exhibited epilation from 10–18 days after irradiations and no skin damage. In the mini-GRID-irradiated animals, the alopecia was concentrated in the small areas corresponding to the peak regions in contrast to the conventionally irradiated animals (Fig. 1c, d).

Longitudinal studies

The longitudinal PET study did not find any statistically significant differences between the three groups (controls, mini-GRID, and conventional RT) at any of the doses or time points looked at (Fig. S2 in supplemental materials).

The MRI study revealed no oedema, inflammation, haemorrhages, or signs of vascular damage in any of the groups at the first dose level (20 Gy) at any time point (Fig. 2). No differences in T2 and T2* brain relaxation times (volumetric or morphological variations) were found among the groups at any of the time points. At 6 months, neither the total brain volume assessment nor the different brain anatomical regions evaluated (cerebral cortex, hippocampus, and corpus callosum) revealed any volumetric differences or morphological variations among the groups. In contrast, the two irradiated groups at 25 Gy show significantly less whole brain volume than the non-irradiated controls (Fig. S3).

Six months after irradiation, all animals irradiated with conventional RT at 25 Gy developed large necrotic lesions that were heterogeneous on the

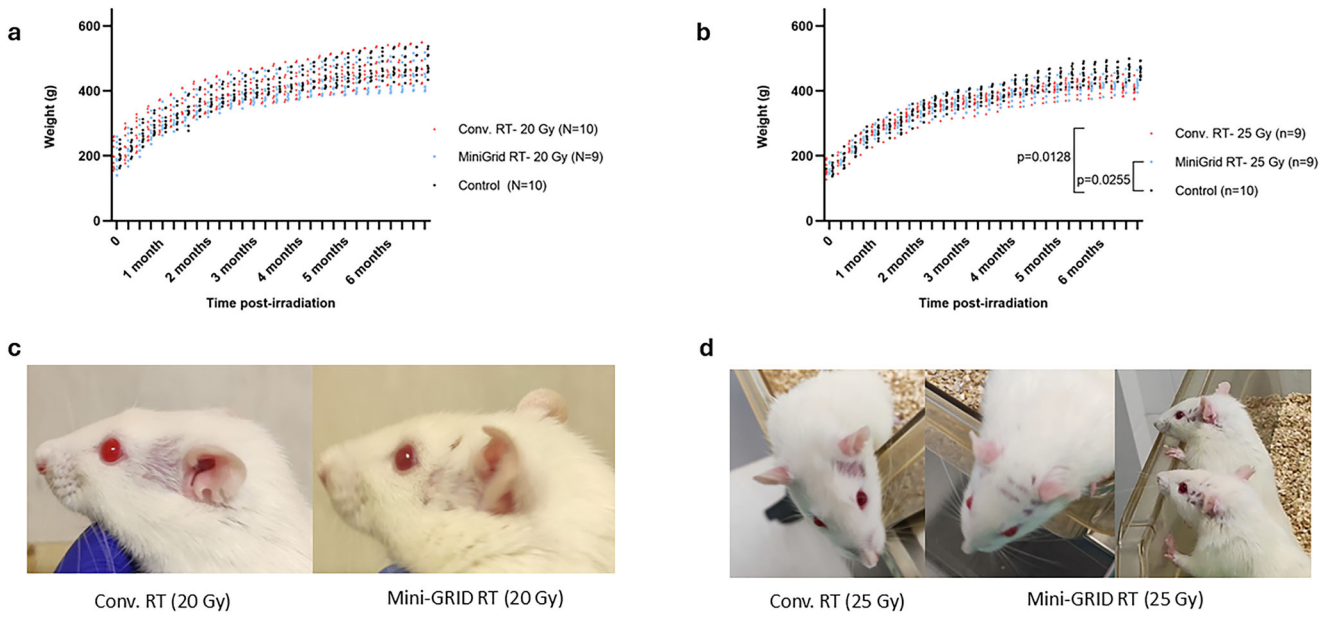

Fig. 1 | Body weights and alopecia in the different groups. a Body weights of the series irradiated with 20 Gy. Gy refers to Gray. **b** Body weights of the series irradiated with 25 Gy. In the latter, the irradiated rats exhibited decreased body weights. Statistical analysis using a Two-way ANOVA test, p values between groups are shown in the graph. **c** Illustration of alopecia 1 month after irradiation in the animals irradiated with 20 Gy. **d** Illustration of alopecia 1 month after irradiation in the animals irradiated 25 Gy. The animals on the left photographs of each column correspond to those who received conventional radiotherapy (Conv.RT), those on the middle or right side to mini-GRID-irradiated animals. Ten or nine animals per group and irradiation mode were included.

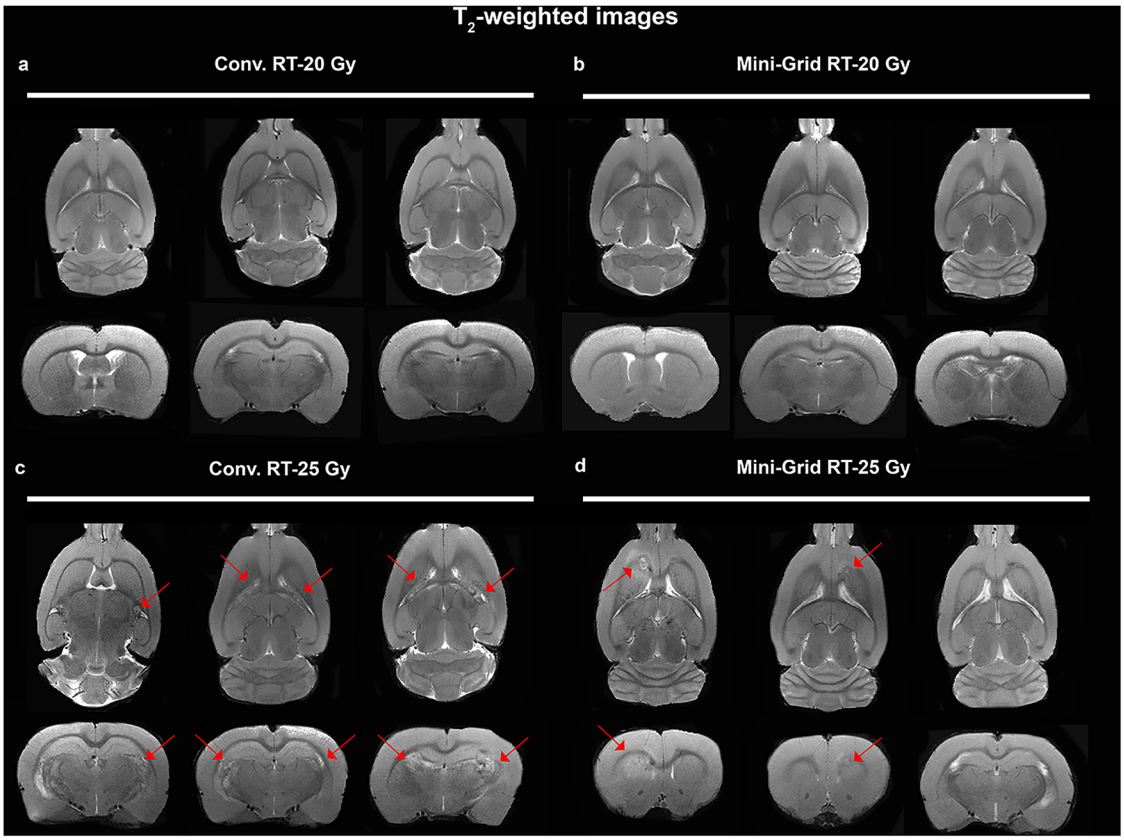

Fig. 2 | Representative MRI images of the different groups of animals. a T2-weighted images for animals who received 20 Gy conventional radiotherapy (conv. RT). Gy refers to Gray. **b** T2-weighted images for animals who received 20 Gy mini-GRID radiotherapy (mini-GRID RT) **c**. T2-weighted images for 25 Gy conventional irradiation. **d** T2-weighted images for 25 Gy mini-GRID irradiation. Radiation necrosis at 25 Gy is heterogeneous on the T2-weighted images and shows large signal enhancement (red arrows).

T2-weighted images (Fig. 2). These lesions were primarily located in the fimbria fornix, striatum, and hippocampal formation. Additionally, one animal exhibited cerebral haemorrhage in the striatum and corpus callosum. On the other hand, necrotic lesions were found in only two animals of the mini-GRID group (40%), one in the striatum and the other in the corpus callosum, both presenting multiple hyperintense areas.

Regarding the lesion volume, the average volume per animal in the mini-GRID group is half that of the conventional RT group ($11.7 \pm 15.5\ mm^3$ vs. $23.9 \pm 16.7\ mm^3$). These results suggest that as the dose increases, brain lesions are larger and more heterogeneous in animals irradiated with conventional RT compared to those irradiated with mini-GRID RT.

Infrared microspectroscopy studies

Figure S4 shows the FTIRM measurements on tissue sections of irradiated animals. Figure 3 shows the probability density of several spectral ratios. Conventionally irradiated animals exhibit an enhanced AI intensity, which has been correlated with modifications in the secondary protein structure[39]. Furthermore, the conventional RT group exhibits reduced PhI and PhII intensities compared to the mini-GRID-irradiated animals, indicating nucleic acid damage and oxidative[40]. Moreover, we observed several modifications in the 3000–2800 cm^{-1} spectral region and in the band located at 1760–1718 cm^{-1}, which were associated with the C=O carbonyl ester stretching vibrations arising from phospholipids. An increase in the C=O carbonyl ester band is observed for both irradiation groups, being slightly higher for the Conv. RT group. This increase was previously correlated as a hallmark of cell death due to oxidative damage[41]. These modifications are concomitant with an increase in the asymmetric methylene to asymmetric methyl aCH_2/aCH_3 spectral ratio (2945–2900 cm^{-1} and 2980–2945 cm^{-1}, respectively) for the Conv. RT group, which could be indicative of a higher degree of oxidative process occurring in response to conventional radiation[42].

Our results indicate different biochemical processes in conventional irradiation with respect to mini-GRID. Mini-GRID therapy appears to lead to changes that are close to those of non-irradiated controls. The results obtained provide valuable insights to investigate further, and more specifically, those changes.

Behavioural studies

Concerning behavioural studies, no differences among the groups were observed. Motor ability, motivation and anxiety were measured by the OF test, finding no differences among the groups or as a function of dose or time (Fig. S5). A novel object recognition test was used as memory assessment. No statistically significant differences were observed (Fig. S6).

Muscular tone is preserved after irradiation. No differences were observed between groups or overtime in any of the doses received by the animals (Fig. S7).

Histopathological evaluation

All irradiated brains, except for one from the mini-GRID-20 Gy group, showed lesions similar in nature but different in intensities compared to the control samples ($n = 18$), which showed no lesions, as depicted in Figs. 4 and S8. The most noticeable injuries were radionecrosis foci, which could be seen as pale, well-defined areas stained with HES. We also observed isolated degenerating neurons, often vacuolated. Numerous Iba-1-positive cells (microgliosis) and GFAP-positive cells (astrocytosis) surround these lesions. Globally, incidences of neuron necrosis and degeneration were respectively 9, 8, 3, and 6 from conventional RT–25 Gy, mini-GRID RT–25 Gy, conventional RT–20 Gy, and mini-GRID– 20 Gy groups. This

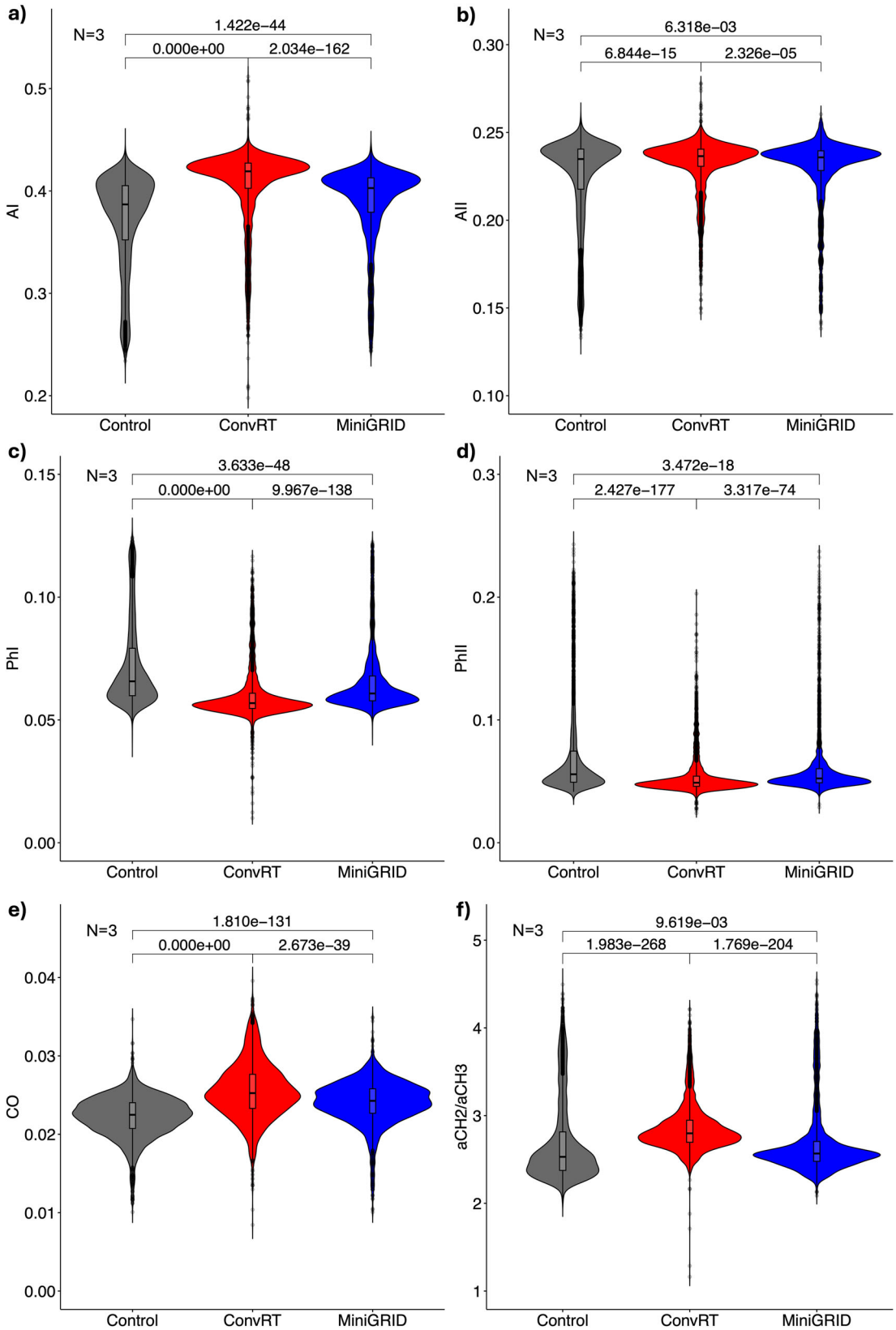

Fig. 3 | Infrared microscopy results. Violin plots showing the distribution of the relative intensities of the following bands: **a** Amide I (AI; 1714–1585 cm^{-1}); **b** Amide II (AII; 1585–1483 cm^{-1}); **c** Phosphate I (PhI; 1270–1186 cm^{-1}); **d** Phosphate II (PhII; 1135–1004 cm^{-1}); **e** C=O carbonyl ester band (CO; 1760–1718 cm^{-1}) with respect to the integration over the 1800–950 cm^{-1} spectral range, and **f** of the asymmetric CH_2 with respect to the asymmetric CH_3 spectral ratio (aCH2/aCH3; 2945–2900 cm^{-1} and 2980–2945 cm^{-1}, respectively). As indicated in the figure, the total number of animals considered is 3 ($N = 3$). Each plot contains more than 3000 points corresponding to the infrared spectrum in each pixel of the brain sections of the animals. Due to the large number of points per animal, they have been omitted from the graph for a correct visualization. The nonparametric Kruskal–Wallis test was employed to assess the significance between the control and irradiated groups. Then, when global group effects were found to be statistically significant, a Dunn test for pairwise comparisons, including the Bonferroni adjustment, was performed. Gy refers to Gray.

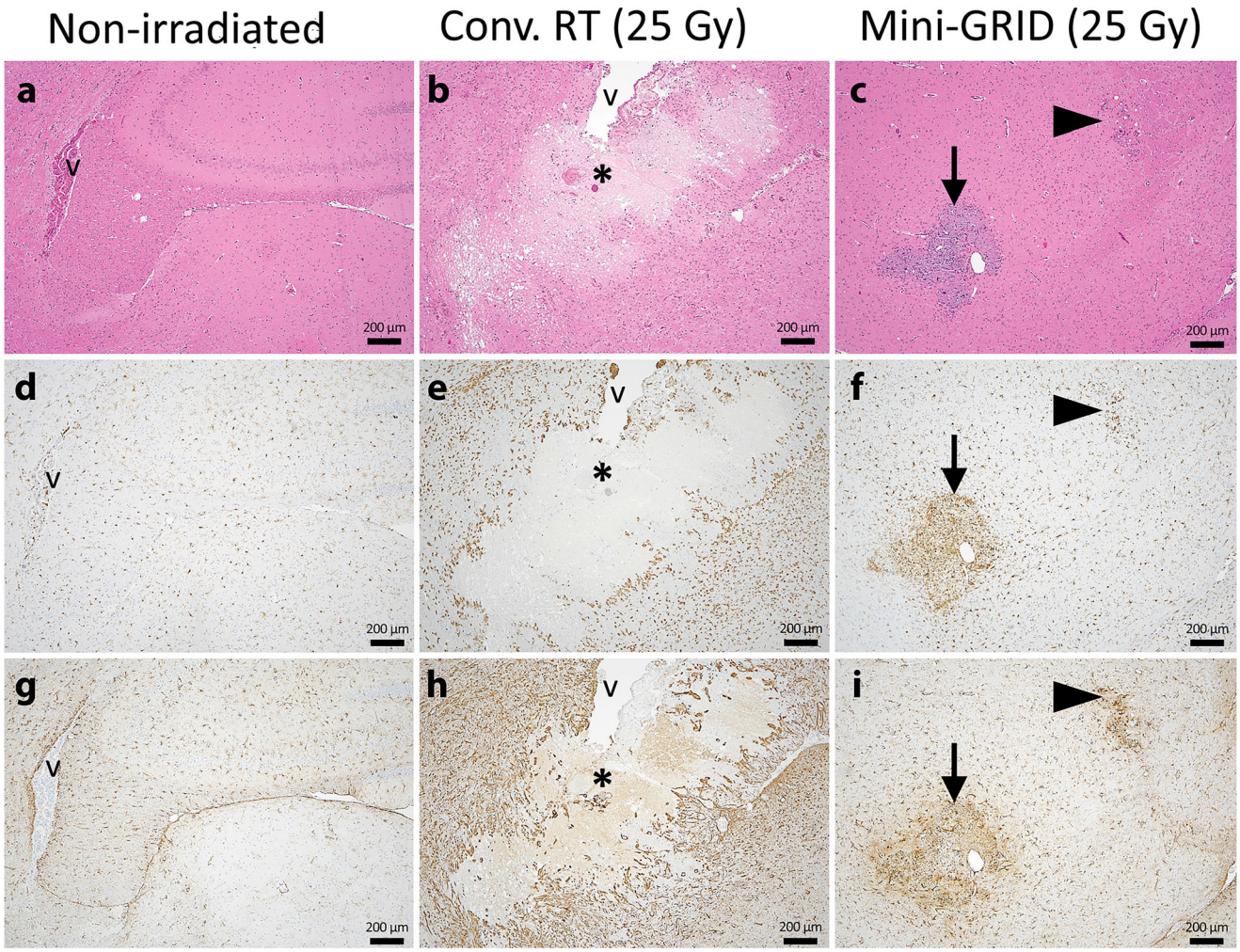

Fig. 4 | Histopathological assessment after radiotherapy at 25 Gy (RT – 25 Gy). The left column displays controls (**a**, **d**, **g**), the central column displays conventional RT (**b**, **e**, **h**), and the right column displays miniGRID (**c**, **f**, **i**). Gy refers to Gray.HE staining is employed in **a**, **b**, **c**; Iba-1 and GFAP stainings are used in **d**, **e**, **f** and **g**, **h**, **I**, respectively. Compared to the control group (**a**), RT (**b**, **c**) caused large pale foci of necrosis (*) that were often close to lateral ventricles (v), foci with neurons and vacuoles that swelled up (arrowhead), and foci that were full of cell debris and had more cells (arrow). These foci and their surroundings were rich in cells positive for Iba-1, which corresponded to microgliosis (**d**–**f**), and in cells positive for GFAP (**g**, **h**, **i**), which corresponded to astrocytosis.

suggests that lesions happen more often after RT 25 Gy compared to RT 20 Gy. t's important to note that at 25 Gy, radionecrosis was severe, bilateral, and linked to large bleeding with conventional RT ($n = 9$). However, with Mini-GRID, radionecrosis looked focal and limited in extension ($n = 5$) or even absent ($n = 1$). We observed thickening of the supportive connective tissue in the choroid plexus from the lateral and 4th ventricles in 9, 4, 5, and 6 samples from the conventional RT–25 Gy, mini-GRID RT–25 Gy, conventional RT–20 Gy, and mini-GRID–20 Gy groups, respectively. Importantly, cellular debris indicative of necrosis was only observed following conventional RT and not mini-GRID. Thus, the results suggested a reduced incidence and severity following mini-GRID RT–25 Gy compared to conventional RT at the same dose.

We scored the following parameters: necrosis, mineralization, choroid plexus alterations, intracellular lipofuscin deposit, astrocytosis based on anti-GFAP IHC, and microgliosis based on anti-Iba1 IHC. A cumulative composite score was calculated for each brain (Fig. 5). Median scores were respectively 0, 12, 8, 3, and 7.5 for the control, conventional RT – 25 Gy, mini-GRID RT–25 Gy, standard RT – 20 Gy, and mini-GRID–20 Gy groups. There was a group effect, and there were big differences between the control group and the Standard RT–25 Gy, mini-GRID RT–25 Gy, and mini-GRID–20 Gy groups in another other hand (Kruskal-Wallis test, $p = 0.0001$; $p = 0.007$ and $p = 0.0036$, respectively). Thus, histologically, we cannot differentiate neurotoxicity at 20 Gy between mini-GRID and conventional RT, but at 25 Gy, we can discern a trend towards increased neurotoxicity with conventional RT compared to mini-GRID ($p = 0.08$). Also similar in nature, degenerating foci were often larger after conventional RT compared to mini-GRID RT at 25 Gy. The serial coronal sections were stained with Hematoxylin-Eosin-Saffron (upper panel), immunolabelling of Iba-1 (intermediate panel), and GFAP (lower panel). The same region is shown for each preparation.

Discussion

RT is a cornerstone of cancer treatment. However, normal tissue tolerances still compromise the effectiveness of clinical radiation therapy (RT) for many late-stage tumours, radio-resistant tumours, recurring tumours, and brain and paediatric tumours. Therapeutic strategies leading to different biological mechanisms than conventional RT could be a game changer for those currently hopeless cases. One of those strategies is SFRT, a therapeutic approach with the potential to disrupt the classical paradigms of conventional radiation therapy. Several decades of clinical use and numerous preclinical experiments suggest that SFRT has the potential to increase the therapeutic index for those cases[9]. The ongoing advancement of both SFRT technology and radiobiology knowledge is generating a growing interest in SFRT worldwide, and the aim of this work was to contribute to the

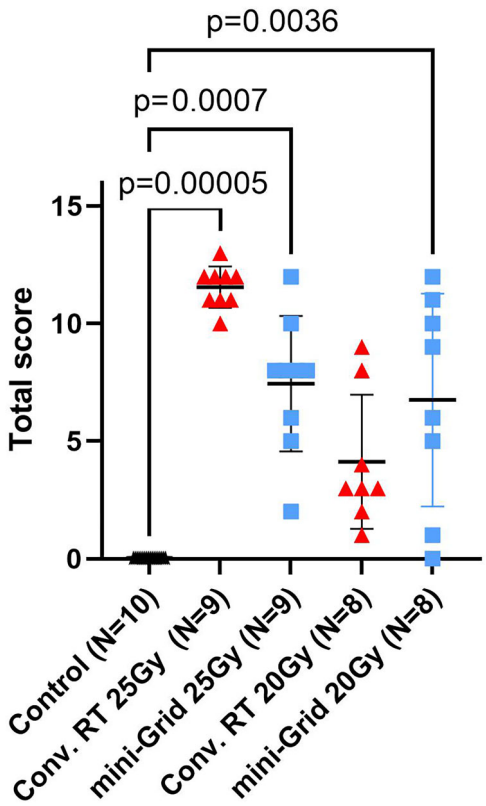

Fig. 5 | Lesion score. Individual value plot showing the cumulative score obtained after evaluation of 6 histological parameters. Median values per group are indicated with a black line and significant results with *p* value (Kruskal-Wallis test). Animals were irradiated with 25 Gy. Gy refers to Gray.

advancement and expansion of the use of SFRT. Among the different forms of SFRT, GRID and LRT have been used to treat numerous patients in conventional medical LINACS[9]. The beam widths (or hot spots) and typical peak doses are around 1 cm^2 and 15–20 Gy, respectively. These characteristics have limited the clinical use of SFRT to bulky tumours and palliative intent.

We studied a new idea called mini-GRID RT to improve the therapeutic index of clinical SFRT and make it a more widely used technique. Our goal was to move SFRT from marginal (and mostly palliative) use to a larger one.

We successfully implemented mini-GRID RT in an FFF LINAC, departing from a previous in silico study. We achieve beam widths of less than or equal to 2 mm^2 in FFF LINACs due to their lower energy spectrum and higher dose rates compared to conventional ones. The use of very narrow beams (1–2 mm^2) allows exploiting the dose volume effects (the smaller the beam size is, the higher the normal tissue tolerances[22]). PVDR values (spatial dose modulation) around 4 are obtained, similar to some other experimental techniques such as proton minibeam radiation therapy, where remarkable normal tissue sparing (brain) is observed[32,37]. Satisfactory peak dose rates of around 7 Gy/min are achieved.

As proof of the concept of this new optimized implementation we have performed an in vivo experiment: rats' brains were irradiated. A large proportion of the brain was irradiated as a conservative approach since if toxicity reduction is observed when large volumes are irradiated, the same can be expected in smaller volume irradiation. The same model was employed in previous proof-of-principles studies of SFRT[37,43].It is a relevant model since the brain is a very radiosensitive organ and several brain tumours are still an unmet medical need (i.e. gliomas). A dose escalation study (20 and 25 Gy) was conducted. No clinical symptoms and no lesions are observed in the longitudinal study (PET, MRI) of the animals receiving 20 Gy. The histopathological evaluation of the 20 Gy series showed a similar neurotoxicity between mini-GRID and conventional RT in terms of focal (micrometric) foci of mineralization in striatum and thalamus, to choroid plexus alteration, to degeneration and necrosis. The observed histological lesions are associated with microglial and astrocytic hyperplasia and activation. No neuroinflammation or astrocytic reactivity is observed at 6 months post-irradiation except for the degenerating/necrotizing areas. Lesion's pattern is concentrated in microscopic (non-extensive) foci, without apparent impact on cognitive, emotional, and motor processes. Thereby, while in the configuration and dose studied, we could not single out major lesional differences between conventional and mini-GRID RT in the follow up time (6 months) of this study, our evaluation indicates that the new optimised GRID therapy allows to use high peak doses, 42 Gy in one fraction, a factor twice higher than the peak doses generally employed in conventional GRID therapy (20 Gy peak dose[9]). No direct comparison could be established with GRID therapy rat brain irradiations since the beam widths employed (1 cm^2) are too large. One single beam would irradiate almost the whole brain, avoiding the evaluation of the effects of the spatial dose fractionation. However, the fact that our study shows a doubling of the peak dose that could be potentially used in an organ so radiosensitive as the brain, offers great promise for future treatments.

The lesions in the conventional RT group are less extensive than in previous works using conventional radiotherapy with low energy x-rays[43], probably linked to a higher RBE of low energy X-rays[44]. Differences between conventional and mini-GRID RT become more evident when the dose is increased to 25 Gy. A net reduction of toxicity is observed in the mini-GRID group, both in the MRI and histological analysis. While all the animals in the conventional group presented extensive and severe brain damage, only around 50% of the mini-GRID irradiated animals showed lesions, which were globally less severe and extensive than in the conventional group, suggesting that 25 Gy is the TD50 (dose where the toxicity occurs in 50% of the cases) for mini-GRID brain irradiations.

No differences among groups were observed in the behavioural tests performed within the timeframe of this study, neither at 20 nor at 25 Gy. However, memory alterations were observed in brain irradiations with conventional proton irradiations at 25 Gy in previous studies[45]. The fact that the same observations were not found in this work could be linked to some differences between the impact of protons and photons, but also to dosimetry uncertainties. The dose in this work was 25 ± 1 Gy, implying that it is possibly that the animals received slightly lower dose, potentially below the threshold to observe some cognitive impairment in the study timeframe.

Regarding potential patients' impact, six-months is already considered long-term concerning this type of evaluations. Our previous studies indicate that memory alteration or anxiety manifest at a time delay equal or shorter than 6 months should they be present[37,45]. It should be noted that the mean life span of a rat is 2 years, thus, 6 months could be compared to 20 years in the life of a patient, which is a long-time span after a brain tumour treatment. However, we cannot exclude some cognitive impairment or anxiety appearing at a later point.

While this study did not intend to be mechanistic, the results of the "probe"-study using infrared microspectroscopy analysis suggest different early biochemical changes in both modalities, with conventional RT leading to stronger modifications in the secondary protein structure and higher oxidative damage than in mini-GRID RT. Structural changes in the proteins were previously attributed to cell death processes due to a different distribution of proteins or to denaturalization of existing proteins[41]. Thus, the results suggest different cell death processes in mini-GRID versus conventional RT. Future studies will assess the implications of those processes in terms of tissular effects (i.e., vascular or immune effects).

Globally, the results of this study show that our optimized GRID therapy might be able to further widen the therapeutic window of SFRT. It could be used with curative intent in radioresistant tumours of quite different sizes, enabling more aggressive dose escalation schemes and, therefore, offering advantages with respect to current SFRT clinical practices. Along this line, Table 2 summarizes the main differences with respect to conventional GRID therapy II. All the potential biological differences

Table 2 | Main differences between GRID and mini-GRID therapies

	GRID	Mini-GRID
Beam width	1 cm^2	1–2 mm^2
Tumour size	Bulky	Small or large
Peak and valley doses	~15–20 Gy/5–8 Gy	~42 Gy/10 Gy; 55 Gy/12.7 Gy
Intention	Mainly palliative	Promising radical treatments

among the two techniques, beyond the dose-volume effects and increase of normal tissue tolerances, require further evaluation.

While this was a first exploratory study performed as a proof of principle, it may contribute to the expansion of SFRT, an intriguing approach with potential to reshape RT. Further biological experiments in tumour-bearing animals are warranted to evaluate the tumour control efficacy of mini-GRID RT in different tumour types.

Data availability

The data will be made available upon reasonable request by contacting the corresponding author. Raw data has been stored in a public repository (figshare, https://doi.org/10.6084/m9.figshare.28046138)[46].

Received: 19 August 2024; Accepted: 14 March 2025;
Published online: 05 April 2025

References

1. Kersting, J. et al. Effect of radiotherapy dose on outcome in nonmetastatic Ewing Sarcoma. *Adv. Radiat. Oncol.* **8**, 101269 (2023).
2. Mahvi, D. A. et al. Local cancer recurrence: the realities, challenges, and opportunities for new therapies. *CA Cancer J. Clin.* **68**, 488–505 (2018).
3. Mohammadi, A. M. et al. Impact of the radiosurgery prescription dose on the local control of small (2 cm or smaller) brain metastases. *J. Neurosurg.* **126**, 735–743 (2017).
4. Lawrie, T. A. et al. Long-term neurocognitive and other side effects of radiotherapy, with or without chemotherapy, for glioma. *Cochrane Database Syst. Rev.* **8**, CD013047 (2019).
5. Singh, R. et al. Dose escalated radiation therapy for glioblastoma multiforme: an international systematic review and meta-analysis of 22 prospective trials. *Int J. Radiat. Oncol. Biol. Phys.* **111**, 371–384 (2021).
6. Minniti, G. et al. Stereotactic radiosurgery for brain metastases: analysis of outcome and risk of brain radionecrosis. *Radiat. Oncol.* **6**, 48 (2011).
7. Vatner, R. E. et al. Endocrine deficiency as a function of radiation dose to the hypothalamus and pituitary in pediatric and young adult patients with brain tumors. *J. Clin. Oncol.* **36**, 2854–2862 (2018).
8. Haddy, N. et al. Relationship between the brain radiation dose for the treatment of childhood cancer and the risk of long-term cerebrovascular mortality. *Brain* **134**, 1362–1372 (2011).
9. Prezado, Y. et al. Spatially fractionated radiation therapy: a critical review on current status of clinical and preclinical studies and knowledge gaps. *Phys. Med. Biol.* **69**, 10TR02 (2024).
10. Yan, W. et al. Spatially fractionated radiation therapy: History, present and the future. *Clin. Transl. Radiat. Oncol.* **20**, 30–38 (2020).
11. Billena, C. & Khan, A. J. A current review of spatial fractionation: back to the future? *Int J. Radiat. Oncol. Biol. Phys.* **104**, 177–187 (2019).
12. Prezado, Y. Divide and conquer: spatially fractionated radiation therapy. *Expert Rev. Mol. Med.* **24**, 12 (2022).
13. Mohiuddin, M. et al. High-dose spatially-fractionated radiation (GRID): a new paradigm in the management of advanced cancers. *Int J. Radiat. Oncol. Biol. Phys.* **45**, 721–727 (1999).
14. Wu, X. et al. The technical and clinical implementation of LATTICE Radiation Therapy (LRT). *Radiat. Res* **194**, 737–746 (2020).
15. Mohiuddin, M. et al. Palliative treatment of advanced cancer using multiple nonconfluent pencil beam radiation. A pilot study. *Cancer* **66**, 114–118 (1990).
16. Neuner, G. et al. High-dose spatially fractionated GRID radiation therapy (SFGRT): a comparison of treatment outcomes with Cerrobend vs. MLC SFGRT. *Int J. Radiat. Oncol. Biol. Phys.* **82**, 1642–1649 (2012).
17. Choi, J. I. et al. Clinical outcomes of spatially fractionated GRID radiotherapy in the treatment of bulky tumors of the head and neck. *Cureus* **11**, e4637 (2019).
18. Amendola, B. E. et al. Safety and efficacy of lattice radiotherapy in voluminous non-small cell lung cancer. *Cureus* **11**, e4263 (2019).
19. Mohiuddin, M. et al. Early clinical results of proton spatially fractionated GRID radiation therapy (SFGRT). *Br. J. Radio.* **93**, 20190572 (2020).
20. Grams, M. P. et al. Minibeam Radiation Therapy Treatment (MBRT): Commissioning and First Clinical Implementation. *Int. J. Radiat. Oncol. Biol. Phys.* **120**, 1423–1434 (2024).
21. Dilmanian, F. A. et al. Response of rat intracranial 9L gliosarcoma to microbeam radiation therapy. *Neuro Oncol.* **4**, 26–38 (2002).
22. ZEMAN, W., CURTIS, H. J. & BAKER, C. P. Histopathologic effect of high-energy-particle microbeams on the visual cortex of the mouse brain. *Radiat. Res* **15**, 496–514 (1961).
23. Bouchet, A. et al. Better Efficacy of synchrotron spatially microfractionated radiation therapy than uniform radiation therapy on Glioma. *Int J. Radiat. Oncol. Biol. Phys.* **95**, 1485–1494 (2016).
24. Fernandez-Palomo, C. et al. Complete remission of mouse melanoma after temporally fractionated microbeam radiotherapy. *Cancers* **12**, 2656 (2020).
25. Prezado, Y. et al. Tumor control in RG2 Glioma-bearing rats: a comparison between proton minibeam therapy and standard proton therapy. *Int J. Radiat. Oncol. Biol. Phys.* **104**, 266–271 (2019).
26. Bertho, A. et al. First evaluation of temporal and spatial fractionation in proton minibeam radiation therapy of glioma-bearing rats. *Cancers* **13**, 4865 (2021).
27. Martínez-Rovira, I., Puxeu-Vaqué, J. & Prezado, Y. Dose evaluation of Grid Therapy using a 6 MV flattening filter-free (FFF) photon beam: A Monte Carlo study. *Med Phys.* **44**, 5378–5383 (2017).
28. Fogliata, A. et al. Flattening filter free beams from TrueBeam and Versa HD units: Evaluation of the parameters for quality assurance. *Med Phys.* **43**, 205 (2016).
29. Ortiz, R., De Marzi, L. & Prezado, Y. Preclinical dosimetry in proton minibeam radiation therapy: Robustness analysis and guidelines. *Med Phys.* **49**, 5551–5561 (2022).
30. Goerzen, D. et al. An MRI-derived Neuroanatomical Atlas of the Fischer 344 Rat Brain. *Sci. Rep.* **10**, 6952 (2020).
31. Ostrom, Q. T. et al. CBTRUS Statistical Report: primary brain and other central nervous system tumors diagnosed in the United States in 2015-2019. *Neuro Oncol.* **24**, v1–v95 (2022).
32. Prezado, Y. et al. Proton minibeam radiation therapy spares normal rat brain: Long-Term Clinical, Radiological and Histopathological Analysis. *Sci. Rep.* **7**, 14403 (2017).
33. Baker, M. J. et al. Using Fourier transform IR spectroscopy to analyze biological materials. *Nat. Protoc.* **9**, 1771–1791 (2014).
34. Martínez-Rovira, I., Seksek, O. & Yousef, I. A synchrotron-based infrared microspectroscopy study on the cellular response induced by gold nanoparticles combined with X-ray irradiations on F98 and U87-MG glioma cell lines. *Analyst* **144**, 6352–6364 (2019).
35. González-Vegas, R. et al. Investigating the biochemical response of proton minibeam radiation therapy by means of synchrotron-based infrared microspectroscopy. *Sci. Rep.* **14**, 11973 (2024).
36. Martínez-Rovira, I. et al. Infrared microspectroscopy to elucidate the underlying biomolecular mechanisms of FLASH radiotherapy. *Radiother. Oncol.* **196**, 110238 (2024).
37. Lamirault, C. et al. Short and long-term evaluation of the impact of proton minibeam radiation therapy on motor, emotional and cognitive functions. *Sci. Rep.* **10**, 13511 (2020).
38. Crissman, J. W. et al. Best practices guideline: toxicologic histopathology. *Toxicol. Pathol.* **32**, 126–131 (2004).

39. Barth, A. Infrared spectroscopy of proteins. *Biochim Biophys. Acta* **1767**, 1073–1101 (2007).
40. Sofińska, K. et al. Molecular spectroscopic markers of DNA damage. *Molecules*. **25**, 561 (2020).
41. Holman, H. Y. et al. IR spectroscopic characteristics of cell cycle and cell death probed by synchrotron radiation based Fourier transform IR spectromicroscopy. *Biopolymers* **57**, 329–335 (2000).
42. Lipiec, E. et al. Synchrotron FTIR shows evidence of DNA damage and lipid accumulation in prostate adenocarcinoma PC-3 cells following proton irradiation. *J. Mol. Struct.* **1073**, 7 (2014).
43. Prezado, Y. et al. Transfer of Minibeam Radiation Therapy into a cost-effective equipment for radiobiological studies: a proof of concept. *Sci. Rep.* **7**, 17295 (2017).
44. Bell, B. I. et al. Orthovoltage X-Rays Exhibit Increased Efficacy Compared with γ-Rays in Preclinical Irradiation. *Cancer Res* **82**, 2678–2691 (2022).
45. Iturri, L. et al. Oxygen supplementation in anesthesia can block FLASH effect and anti-tumor immunity in conventional proton therapy. *Commun. Med.* **3**, 183 (2023).
46. Prezado et al. dx.https://doi.org/10.6084/m9.figshare.28046138

Acknowledgements

This study was sponsored by VARIAN, a Siemens Healthineers Company. IMR acknowledges the support of the Spanish Ministry of Science, Innovation, and Universities (Grants RYC2018-024043-I, PID2023-146939OB-I00, and PRE2021-097298). YP warmly thanks Thongchai Masilela for his help with the AutoCAD drawing of the collimator. Ramón Iglesias-Rey (CP22/00061) acknowledges funding from the Miguel Servet Programme of the Instituto de Salud Carlos III and is co-financed by the EU. We warmly thank Anxo Vidal and CEBEGA for their support to this project.

Author contributions

Conceptualization of the study (Y.P.), study supervision (Y.P.), study design (Y.P.), funding (Y.P.), behavioural tests (C.L., M.A.), histology (T.L., E.B.), irradiations (M.S.G., V.L.), dosimetry (M.S.G., T.S.), MRI studies (R.I., S.F.R.), Infrared studies (I.M.R., I.Y., R.G., M.J.), PET studies (P.A., N.G.L.), scientific discussions (M.P., A.G.C., Y.P.), animals daily follow up (MA), data curation (CL, MA, YP), manuscript writing (YP).

Competing interests

This work has been funded by VARIAN, a Siemens Healthineers Company.

Additional information

Supplementary information The online version contains supplementary material available at https://doi.org/10.1038/s43856-025-00809-7.

Correspondence and requests for materials should be addressed to Yolanda Prezado.

Peer review information *Communications Medicine* thanks the anonymous reviewers for their contribution to the peer review of this work.

Reprints and permissions information is available at http://www.nature.com/reprints

Publisher's note Springer Nature remains neutral with regard to jurisdictional claims in published maps and institutional affiliations.

[1]New Approaches in Radiotherapy Lab, Center for Research in Molecular Medicine and Chronic Diseases (CIMUS), Instituto de Investigación Sanitaria de Santiago de Compostela (IDIS), University of Santiago de Compostela, A Coruña, Spain. [2]Translational Research Department, Institut Curie, Experimental Radiotherapy Platform, Université Paris Saclay, Orsay, France. [3]UMR703 - PAnTher - APEX, Oniris, Nantes, France. [4]Institut Curie, Université PSL, CNRS UMR3347, Inserm U1021, Signalisation Radiobiologie et Cancer, Orsay, France. [5]Université Paris-Saclay, CNRS UMR3347, Inserm U1021, Signalisation Radiobiologie et Cancer, Orsay, France. [6]Neuroimaging and Biotechnology Laboratory (NOBEL), Clinical Neurosciences Research Laboratory (LINC), Health Research Institute of Santiago de Compostela (IDIS), Santiago de Compostela, Spain. [7]Molecular Imaging and Pharmacokinetic Modelling Group, Center for Research in Molecular Medicine and Chronic Diseases (CiMUS), University of Santiago de Compostela, Spain; Nuclear Medicine and Molecular Imaging Group, Health Research Institute of Santiago de Compostela (IDIS), University Hospital Santiago de Compostela, Santiago de Compostela, Spain. [8]Physics Department, Universitat Autònoma de Barcelona (UAB), 08193 Cerdanyola del Vallès, Barcelona, Spain. [9]MIRAS Beamline, ALBA Synchrotron, 08209 Cerdanyola del Vallès, Barcelona, Spain. [10]Department of Radiation Oncology, Hospital Clínico Universitario Santiago de Compostela, Santiago de Compostela, Spain. [11]Department of Medical Physics, Complexo Hospitalario Universitario de Santiago de Compostela, Santiago de Compostela, Spain. [12]Oportunius Program, Galician Agency of Innovation (GAIN), Xunta de Galicia, A Coruña, Spain.
✉e-mail: Yolanda.prezado@usc.es